Materials Advances

ROYAL SOCIETY OF CHEMISTRY

PAPER

View Article Online
View Journal

Cite this: DOI: 10.1039/d5ma00717h

Green synthesized cerium oxide nanorods using *Curcuma longa* extract for response surface methodology-based photocatalytic degradation application

Jawayria Najeeb,[a] Sadia Akram,*[a] Sumaira Naeem,[b] Hummera Rafique,*[a] Muhammad Tayyab[c] and Zara Mukaddas[a]

In this study, green fabrication of cerium oxide (CeO_2) nanoparticles (CNRs) was achieved by utilizing *Curcuma longa* extract. The fabricated CNRs were characterized using scanning electron microscopy (SEM), transmission electron microscopy (TEM), X-ray diffraction (XRD), ultraviolet-visible spectroscopy (UV-VIS), and Fourier transform infrared spectroscopy (FTIR). It was observed that the CNRs exhibited a rod-like morphology with a mean length and width of ~13.1 nm and 4.9 nm (assessed *via* TEM micrograph), respectively. The presence of the characteristic diffraction peak of (111) in the XRD analysis also validated the successful fabrication of CNRs. The surface functionalization of the CNRs confirmed that several functional moieties were available on the surface of the CNRs, which enhances the application potential of the CNRs. The synthesized CNRs were utilized for performing the photocatalytic degradation (PD) of norfloxacin (NFX; antibiotic pollutant) by using the response surface methodology (RSM) technique. The reaction was analyzed by utilizing statistical key regressive parameters for the development of a reaction-specific central composite design (CCD)-based model. The CCD model was further tested and validated by using the analysis of variance (ANOVA), normal probability, actual vs predicted PD% value plots, *etc.* The diagnostics and validity revealed that the quadratic model (with a *p*-value of <0.0001 and an R^2 value of 0.9285) exhibited the best fit for representing the PD of NFX. The reaction was optimized considering several criteria. The degradation value of 92.31% was acquired using a CCD-based quadratic model with the optimized parameters of reaction time = 36.31 min, CNR dose = 39.56 mg L^{-1}, NFX dose = 54.52 ppm, and pH = 5.26. The current study underscores the significance of green methodologies for synthesizing morphology-specific nanomaterials and using RSM for analyzing the underlying reactions in detail.

Received 7th July 2025,
Accepted 29th August 2025

DOI: 10.1039/d5ma00717h

rsc.li/materials-advances

1. Introduction

The excessive and persistent introduction of organic pollutants, particularly antibiotics and herbicides, into potable-water reservoirs has emerged as one of the major challenges of recent times, driven by global agricultural and industrial expansion.[1] These hazardous contaminants not only aesthetically damage the ecosystem, but their toxicity and high persistence also damage the aquatic environment and human health.[2] Owing to the unavoidable usage of antibiotics for combating the adverse impacts of microbes, antibiotics have emerged as the most significant class of emerging organic pollutants in recent aquatic profiles. Norfloxacin (NFX) is a well-known broad-spectrum fluoroquinolone antibiotic that is utilized to treat both Gram-positive and Gram-negative bacterial infections associated with human and veterinary care.[3] The ingestion of a high dose of NFX has been known to cause peripheral neuropathy, tingling, tendonitis, depression, hypoglycemia, worsening myasthenia gravis, and aortic aneurysm.[4] In a recent alarming case study, significantly high doses of NFX, *i.e.* 9.4 to 170 ng L^{-1} and 33 to 1150 ng L^{-1} were recorded in treated effluent (from a sewage treatment plant) and surface water reservoir samples, respectively. The samples under study were collected by the authors from several countries, including China, Greece, Sweden, France, Poland, Switzerland, Canada, the Czech Republic, Japan, Australia, the USA, and Italy.[5]

[a] *Department of Chemistry, University of Gujrat, Gujrat-50700, Pakistan. E-mail: jawayria@uog.edu.pk, dr.sadia@uog.edu.pk, humera.qau@gmail.com, mukaddas.zara123@gmail.com*
[b] *Department of Chemistry, Baba Guru Nanak University, Nankana Sahib, 39100, Punjab, Pakistan. E-mail: sumaira.naeem@bgnu.edu.pk*
[c] *Institute of Materials Research, Tsinghua Shenzhen International Graduate School (SIGS), Tsinghua University, Shenzhen, 518055, China. E-mail: m.tayyab72@yahoo.com*

Consequently, the elimination of such toxic pollutants from potable reservoirs is a pressing importance.

A number of removal methodologies, including advanced oxidation processes (AOPs),[6] adsorption,[7] membrane filtration,[8] biodegradation,[9] catalysis,[10] and photocatalysis,[11] have been documented for the elimination of NFX. The AOPs suffer from serious drawbacks, including the utilization of harmful agents, costly arrangement setups, and costly rawmaterials.[12] The adsorption process is also fundamentally questioned, as without carrying out a pollutant recovery step, the adsorption process simply becomes the removal of the pollutant from one medium to another medium (the adsorbent).[13,14] Although membrane filtration is robust and economical, this process is not viable for long-term use, as the reuse capability of the membranes is quite low.[15] The biodegradation method is ineffective because the fluoroquinolone-based antibiotics are highly persistent and do not undergo complete degradation in the ecosystem.[16] Photocatalytic processes are typically highly regarded for dealing with persistent pollutants due to their advantages of high efficacy of degradation, utilization of renewable resource energy (*i.e.* sunlight), the fabrication of low-cost green catalysts, and the complete degradation of NFX.[17] Therefore, a photocatalytic procedure was selected for the degradation of NFX in this study.

For the fabrication of the photocatalytic materials, nanomaterials (NMs) of cerium oxide (CeO_2) were selected to carry out the degradation of NFX. The selection of the CeO_2-NMs was done while keeping in mind the following research gaps identified for this particular material: (a) the synthesis of cerium oxide is typically challenging and requires extremely high temperatures for the fabrication. Numerous researchers have established that high temperatures of $\sim$600 °C along with complicated autoclave and calcination procedures are required for the development of CeO_2-NMs.[18–20] Moreover, achieving a suitable morphology, such as nanoparticles or nanorods, also requires selective reaction conditions. For instance, Akram *et al.*[21] established that without autoclave conditions, CeO_2-nanorod (CNR) fabrication was quite difficult to achieve. Other less extreme reaction methodologies (such as green methodology,[22] chemical co-precipitation,[23] *etc.*) resulted in spherical nanoparticles (NPs) rather than the rod-like morphology. The acquisition of the rod-like morphology by using green methodology (where environmentally friendly biomass is utilized to remove the hazardous fabrication agents) has been scarcely documented and is considered quite a difficult assignment.[24] Considering these research gaps, a green synthetic approach has been modified to fabricate CNRs here under less extreme conditions in comparison to the conventional synthetic route.

Plant-mediated synthesis is the most well-known approach among the documented green approaches, owing to its advantages of simplicity and resource abundance. Several plants, including *Melissa officinalis*, *Hypericum perforatum*,[25] *Zingiber officinale*,[26] *Portulaca oleracea*,[27] have been documented for the preparation of CeO_2-NPs. However, it was observed that the preparation of the CeO_2-NMs, particularly CNRs, using the above-mentioned extracts was not achieved, and the inverse micro-emulsion-based polymerization methodology has to be utilized for the fabrication of CNRs.[28] After extensive trial-and-error experiments, the extract of a flowering plant of *Curcuma longa* (turmeric) was selected for further processing due to its documented richness in phytochemicals.[29] In an agricultural country like Pakistan, *Curcuma longa* is a household spice that is grown abundantly in all the regions of Pakistan. In a recent study done by Canbolat and Ates,[30] the authors documented that total phenolic content (mg GAE g^{-1}) and total flavonoid content (TFC; mg RE g^{-1}) values of 24.74 and 13.54 for Pakistani samples, indicating a high number of phenols and flavonoids are present in this plant. The presence of the phenols, flavonoids, alcohols, and other phytochemicals in the extract was previously documented to be responsible for the preparation and stabilization of NMs;[2] therefore, *Curcuma longa* was selected for the fabrication of CNRs by utilizing the green synthesis approach.

The preparation of CeO_2-NPs using *Curcuma longa* has been recently documented by Gunasekaran *et al.*[31] in the year 2023. However, the fabrication of CNRs using the *Curcuma longa* extract has not yet been documented in the literature. Moreover, the applicability potential of the CNRs is yet to be investigated by using the model reaction of photocatalytic degradation (PD) of NFX. The pollutant NFX is also one of the scarcely studied pollutants. Consequently, the use of NFX for PD *via* CNRs and response surface methodology (RSM) as a means to optimize the PD reaction both adds to the novelty of the article.

2. Materials and methods

2.1. Materials

The chemicals, including cerium nitrate ($Ce(NO_3)_3{\cdot}6H_2O$; analytical grade; 99.99%), ethanol (C_2H_5OH; spectrophotometric grade; 95.0%), norfloxacin ($C_{16}H_{18}FN_3O_3$; analytical grade; $\geq$98.0%), sodium hydroxide (NaOH; reagent grade; $\geq$98.0%), 2-propanol (C_3H_8O; analytical grade; $\geq$99.7%), benzoquinone ($C_6H_4O_2$; reagent grade; $\geq$98.0%), and ethylenediaminetetraacetic acid (EDTA; purified grade; $\geq$98.5%), were procured from MilliporeSigma (formerly Sigma-Aldrich).

2.2. Preparation of turmeric-stabilized CNRs

For the preparation of green CNRs, the modified green methodology previously reported by our group was utilized.[2] Turmeric rhizomes were collected from the local botanical garden of the University of Gujrat, Pakistan. The rhizomes were properly washed and dried in sunlight for three days. The acquired rhizomes were ground to a fine powder and stored in air-tight zip-lock bags for further usage. For the preparation of CNRs, a concentrated turmeric rhizome-based extract was freshly prepared before the start of the experiment. 15 g of turmeric rhizome were dissolved in 200 mL of distilled water, and the reaction mixture was continuously stirred for 36 h. Filtration was done to acquire the turmeric extract for the next step. In a separate titration flask, 2 mM of $Ce(NO_3)_3$ was prepared, and 20 mL of this solution was introduced into

200 mL of turmeric extract. The reaction medium was subjected to continuous stirring at a constant temperature of 70 ± 2 °C for 12 h. Centrifugation was performed to separate the precipitates from the mixture, and the precipitates were successively washed with ethanol and distilled water numerous times to remove impurities. Oven drying of the precipitates was done at 135 °C for one and a half hours. The developed CNRs were also stored in air-tight zip-lock bags for further processing.

2.3. Characterization

The bandgap characteristics of the CNRs and the progression of the model reaction of PD of NFX were investigated using ultraviolet-visible spectroscopy (UV/VIS; PerkinElmer-LAMBDA; Model-3500; US). X-ray diffraction (XRD; Bruker Corporation; Model: D-8-Advance; USA) was utilized to investigate the crystallographic patterns of the CNRs. The surface characteristics associated with the CNRs were studied *via* scanning electron microscopy (SEM; Hitachi; Model: S-4800; Japan), and the size estimation of the CNRs was performed by high-resolution transmission electron microscopy (HR-TEM; ThermoFischer Scientific; Model: FEI-Tecnai G-2; US). Potassium bromide pellet-based analysis of the CNRs was performed to acquire the Fourier Transform Infrared spectroscopic (FTIR; Agilent Technologies, Inc; Model: Carry-630; US) results.

2.4. RSM-based PD of NFX by using CNRs

In order to optimize the specific response (*i.e.* photocatalytic degradation; PD) influenced by a number of exogenous variables, RSM appears to be one of the widely utilized statistical approaches. In fact, this technique is preferred over the OFAT approach as the relationship between the input variables and response is studied and validated *via* the use of a combination of statistical and mathematical modeling in RSM. To develop the required RSM model, the selection of the working levels associated with the variables is extremely crucial. In this study, five different levels, including ±α, ±1, and 0, were selected as the coding levels for the central composite design (CCD) model. The utilized equation for developing the coding levels is presented as eqn (1).

$$Z = \frac{z - \left[\frac{z_{\max} + z_{\min}}{2}\right]}{\left[\frac{z_{\max} - z_{\min}}{2}\right]} \quad (1)$$

Here, Z, z, $z_{\min}$, and $z_{\max}$ represent the factorial code, actual factor value, minimum factor value, and maximum factor value, respectively. The Design Expert software (version 11) was utilized to develop the CCD model for carrying out the PD of NFX. The variables that were investigated *via* the RSM approach for the reaction under study were reaction time (X1; min), CNR dose (X2; mg L^{-1}), NFX dose (X3; ppm), and pH (X4; units). The relationship of these factors with the PD was investigated by considering the levels of ($-\alpha$, -1, 0, +1, $+\alpha$). The details associated with the factors used for CCD design are summarized in Table 1.

Table 1 Summary of the factors, ranges, units, and working levels of ($-\alpha$, -1, 0, +1, $+\alpha$)

Variables	Units	$-\alpha$	Low (-1)	0	High (+1)	$+\alpha$
Reaction time (X1)	min	25.00	30.00	35.00	40.00	45.00
CNR dose (X2)	mg L^{-1}	10.00	20.00	30.00	40.00	50.00
NFX dose (X3)	ppm	12.50	30.00	47.50	65.00	82.50
pH (X4)	units	2.50	5.00	7.50	10.00	12.50

The CCD-developed design for the PD of NFX is presented in Section 3.2.1. The methodology employed for the optimization of the PD of NFX using the CNRs is presented in Fig. 1.

2.5. RSM-CCD design and statistical analysis

The CCD design-based second-order polynomial equation utilized for optimizing the PD of NFX is presented in eqn (2).

$$\mathrm{PD} = \gamma_o + \sum_{i=1}^{k} \gamma_i X_i + \sum_{i=1}^{k} \gamma_{ii} X_i^2 + \sum_{i=1}^{k-1} \sum_{j=2}^{k} \beta_{ij} X_i X_j + \epsilon \quad (2)$$

where PD is the specific response, and the terms γ_o, γ_i, γ_{ii}, and γ_{ij} represent constant, linear, square, and combination/interaction effects, respectively, associated with the reaction under study. The subscripts i and j represent any of the independent factors under study, with the condition that $i \neq j$. Modifying the above equation with respect to the parameters of this study resulted in the generation of eqn (3).

$$\begin{aligned}\mathrm{PD} = {} & \gamma_o + \gamma_1 \mathrm{X1} + \gamma_2 \mathrm{X2} + \gamma_3 \mathrm{X3} + \gamma_4 \mathrm{X4} + \gamma_{12} \mathrm{X1X2} \\ & + \gamma_{14} \mathrm{X1X4} + \gamma_{23} \mathrm{X2X3} + \gamma_{24} \mathrm{X2X4} + \gamma_{34} \mathrm{X3X4} \\ & + \gamma_{11} \mathrm{X1}^2 + \gamma_{22} \mathrm{X2}^2 + \gamma_{33} \mathrm{X3}^2 + \gamma_{44} \mathrm{X4} + \epsilon\end{aligned} \quad (3)$$

where the term ε represents the cumulative error value associated with the performed reaction. Regressive analysis (based on the ordinary least squares technique) was carried out to estimate the fitting of the acquired CCD standard table results with respect to the different models (including linear, cubic, quadratic, and two-factor interaction (2FI)). The statistical parameters, including the coefficient of determination (R^2), adjusted-R^2, predicted-R^2, probability (p)-value, F-test, and lack-of-fit, were utilized to assess the fitting extent of the selected model. ANOVA analysis was also implemented for the validation of the selected CCD model.[32]

2.6. Experimental section

In a distinctive PD reaction, 100 mL of the specific doses of NFX and CNRs (as specified by the CCD standard table) were taken in a photocatalytic reactor (300 W; tungsten-halogen lamp; UV lamp). Sonication was performed for 15 min before performing the illumination step. The start of the PD reaction of NFX was marked by the moment when the lamp was turned ON. The reaction was allowed to complete for the specific reaction time as specified by the CCD table. The absorbance at the start (A_o) of the PD reaction and the absorbance at any instant (A_t) were calculated using the UV/VIS spectrophotometer operating at the

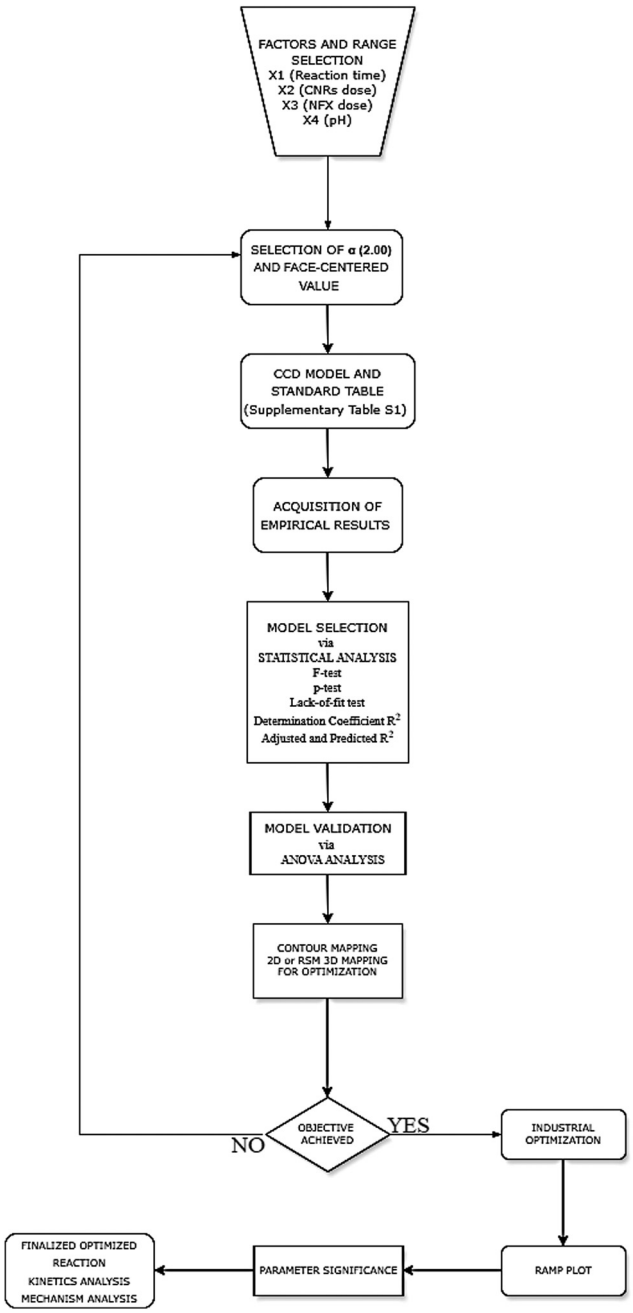

Fig. 1 Design methodology for the RSM-based optimization of PD of NFX.

λ_{max} of NFX (*i.e.* 238 nm). The PD of NFX is presented as eqn (4).

$$PD = \frac{A_0 - A_t}{A_o} \times 100 \quad (4)$$

The impact of different scavengers, including ascorbic acid, chloride, nitrate, and isopropanol, on the numerous free radicals, including superoxide radicals, holes, electrons, and hydroxyl radicals, respectively, involved in the PD mechanism of NFX was also estimated for mechanism studies. The sum of squares (SS) results acquired *via* ANOVA were utilized for the calculation of the total percentage contribution (TPC) of each term with respect to the specific model term, as presented in eqn (5)–(7). The TPC of the parameter can be calculated as follows:

$$TPC_Z = \frac{\sum_{i=1}^{K} SS_i}{\sum_{i=1}^{K}\sum_{i=1}^{K} SS_i + SS_{ii} + SS_{ij}} \times 100 \quad (5)$$

$$TPC_{ZZ'} = \frac{\sum_{i=1}^{K}\sum_{i=1}^{K} SS_{ij}}{\sum_{i=1}^{K}\sum_{i=1}^{K} SS_Z + SS_{ii} + SS_{ij}} \times 100 \quad (6)$$

$$TPC_{ZZ} = \frac{\sum_{i=1}^{K}\sum_{i=1}^{K} SS_{ii}}{\sum_{i=1}^{K}\sum_{i=1}^{K} SS_i + SS_{ii} + SS_{ij}} \times 100 \quad (7)$$

where the subscripts *i*, *ii*, and *ij* represent the individual, quadratic, and combination/interaction terms, respectively, for the specified parameters.[2]

3. Results and discussion

3.1. Characterization of CNRs

The morphological features associated with the CNRs were investigated by utilizing the SEM and TEM micrographs of the sample. The surface properties of the developed CNRs were estimated at different length scales of 500 nm and 1 μm by using SEM analysis as presented in Fig. 2A and B, respectively. At a larger scale of 1 μm, a flower-like morphology was observed. However, increasing the resolution to the length scale of 500 nm indicated that clustered rod-like CNRs were formed using the biogenic turmeric extract. The appearance of the aggregated rod-like structures was anticipated, as morphology modulation *via* a green approach is extremely challenging. Moreover, the utilization of a crude extract of turmeric (containing a number of phytochemicals, including alkaloid, phenol, tannin, saponin, steroid, and flavonoids, *etc.*[33]) and lower temperature values also contributed to the aggregation of the CNRs.

The rod-like morphology was further investigated by using the TEM micrographs taken at 2 nm and 50 nm, as presented in Fig. 3A and B, respectively. The aggregated and separated rods can be clearly seen in the TEM micrographs of the CNRs at the length scale of 50 nm. It was observed that the length of the CNRs was found to be lower than 50 nm. The ImageJ software

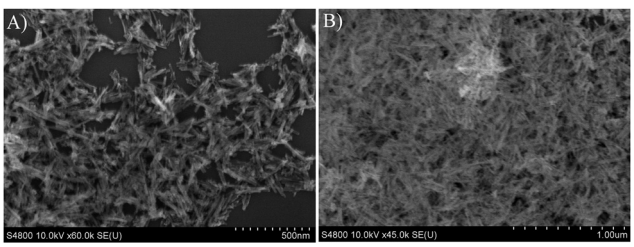

Fig. 2 SEM micrographs of the CNRs at (A) 500 nm and (B) 1 μm.

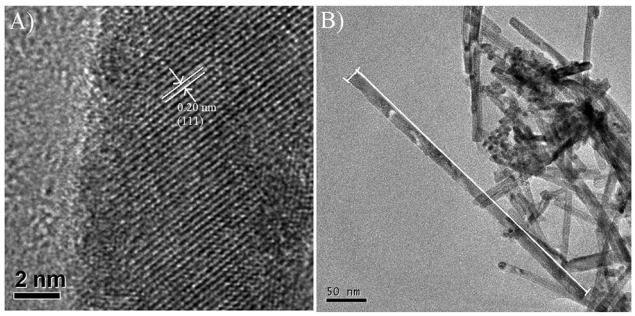

Fig. 3 (A) HRTEM micrograph of the CNRs at the scale of 2 nm and (B) TEM micrograph of the CNRs at the scale of 50 nm.

was utilized to evaluate the length and width of the prepared CNRs. The scaling procedure done on a single nanorod is demarcated by the white line in Fig. 3B. The mean length and width of the CNRs were found to be 13.1 nm and 4.9 nm, respectively. The (111) diffraction plane can also be visualized in the HRTEM micrograph of the CNRs taken at a scale of 2 nm. The XRD analysis further validated the presence of the diffraction plane of (111) in the CNRs, which is primarily responsible for their rod-like morphology.[34]

The XRD analysis of the CNRs (Fig. 4) further validated the successful fabrication of CNRs. The acquired XRD pattern exhibited a 97% match with the COD file # 96-434-3162 associated with the pure ceria crystallographic pattern, as investigated *via* X'Pert HighScore Plus software. The peak list matching screenshot is provided as the SI (Fig. S1). This observation indicated that a highly pure mono-phase (cubic crystallographic system) was successfully synthesized using the aforementioned protocol. The acquisition of diffraction planes at 2θ values of 28.582° (111), 33.103° (200), 47.458° (220), 56.345° (311), 59.041° (222), and 69.934° (400) corresponded quite well with the cubic crystal system of the CNRs. The purity of the synthesized CNRs was also confirmed as no un-indexed diffraction plane associated with any other CNR phase or any other impurities was detected in the XRD pattern of the CNRs.[35] The lattice parameters associated with the cubic phase CNRs were found to be $a = b = c = 5.47$ Å; $\alpha = \beta = \gamma = 90°$; and a volume of 163.44 Å^3. The Debye–Scherrer formula was utilized to estimate the crystallite size (d) of the prepared CNRs. The utilized formula for this purpose is presented in eqn (8).

$$d = \frac{\kappa\lambda}{\mathrm{FWHM}\cos\theta} \tag{8}$$

where the terms κ, λ, and FWHM denote the Scherrer constant, wavelength of Cu k-alpha (0.154 nm), and full width half maximum value associated with the most intense diffraction plane of the CNRs, *i.e.* (111), respectively. The d value for the CNRs was calculated to be 20.74 nm by using the Scherrer equation.

The UV/VIS analysis and the band gap analysis of the CNRs are presented in Fig. 5A and B, respectively. As indicated in Fig. 5A, no absorption peak was observed in the UV/VIS analysis of the turmeric extract, indicating the absence of active UV/VIS species in the extract. This assumption might be false owing to the limitations associated with the colored dispersions analyzed in the UV/VIS instrument. The yellowish-orange extract of the turmeric had to be extensively diluted up to 50 mL to acquire an absorbance value within the acceptable analytical range (*i.e.* 0 to 1.00 a.u.). This dilution may lower the concentration of any UV/VIS active phytochemicals present in the extract, resulting in the absence of the observance of any characteristic peaks in the UV/VIS analysis. The acquisition of the characteristic absorbance value at 307.23 nm also validates the successful synthesis of the CNRs in the reaction medium.[36] The band gap (E_g) analysis of the CNRs was also performed using the Tauc formula presented in eqn (9).

$$(\alpha h\nu)^2 = A(h\nu - E_g) \tag{9}$$

where, α, $h\nu$, and A represent the optical constant, energy of a photon (Planck's constant × frequency), and transition constant, respectively. The E_g value of the CNRs was found to be 3.64 eV, indicating that the CNRs can effectively utilize UV region-based radiation. This was also confirmed by the acquisition of the maximum absorbance peak in the UV region (100–400 nm) exhibited by the CNRs in Fig. 5A. This observation led to the utilization of a UV lamp for the further photocatalytic experiments performed for the degradation of NFX.

The FTIR results of the CNRs and the *Curcuma longa* extract are also summarized in Table 2. As indicated by the FTIR results, the turmeric extract contained several phytochemicals (including phenols, alcohols, carboxylic acids, amines, aromatic phytochemicals, and aliphatic phytochemicals), which can be utilized for the synthesis of CNRs. The slight deviation in the FTIR results of the CNRs from those of the *Curcuma longa* extract indicated that the phytochemicals interacted quite strongly with the CNRs, and the surface of the CNRs was found to be functionalized with many functional moieties. This functionalization is significant as it will also contribute towards the PD of NFX by developing numerous interactions with the NFX molecules.

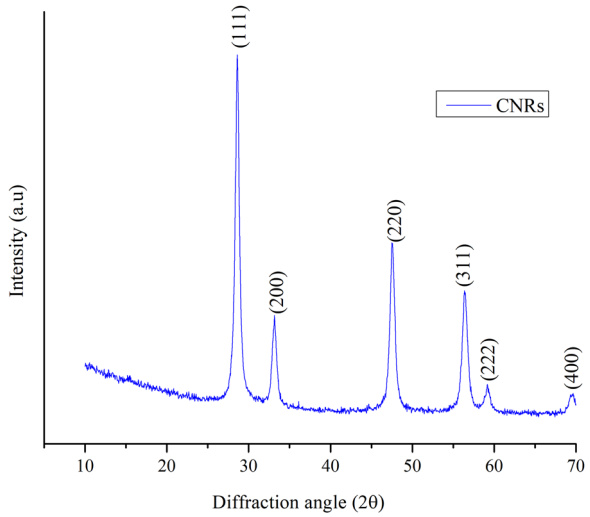

Fig. 4 XRD analysis of the CNRs.

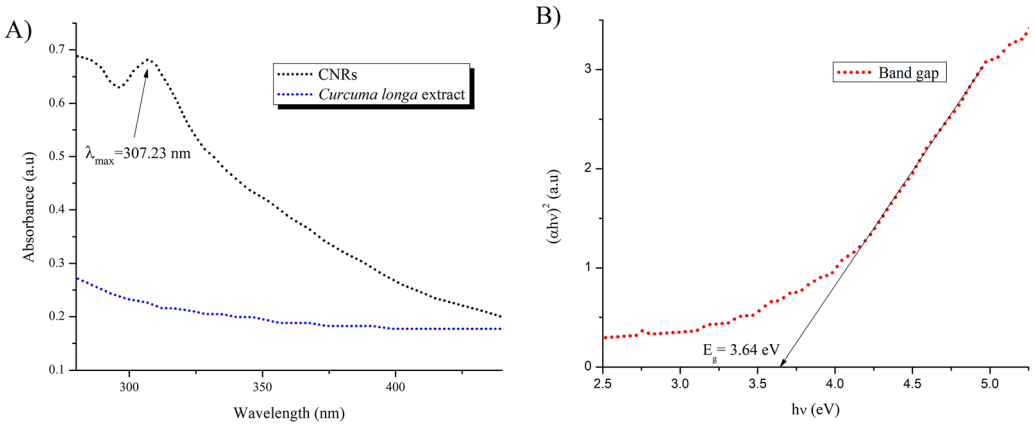

Fig. 5 (A) UV/VIS analysis and (B) Tauc plot analysis of the CNRs.

Table 2 FTIR analysis of the CNRs and *Curcuma longa* extract

Observed frequency (cm^{-1})			
CNRs	*Curcuma longa* extract	Main bond	Comparison of the FTIR findings with the relevant literature
3355.36	3339.81	ν (–OH)	37
2780.71	2958.78	ν (–CH)	38
2570.76	—	ν (–CH)	37
2104.97	2073.87	δ (–COOH)	27
1631.41	1623.63	δ (–NH)	37
1531.35	1530.32	ν (–C═O)	37
1450.62	1452.54		27
1375.51	1382.71	δ (–CH)	39
1256.85	1258.94	ν (–CC–)	27
1235.84	1196.73	ω ($–CH_2$)	27
1150.07	1142.30	δ (–OCH), δ (–C═O)	37
777.60	738.32	ν (–C–O)	38
567.65	579.86	δ (–COC)	37
514.52	—	(Ce–O–Ce)	27

ν, δ, and ω denote the stretching, bending, and wagging frequencies

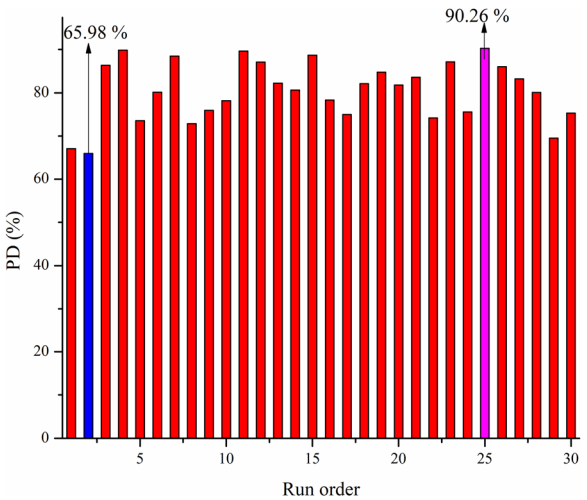

Fig. 6 4-Factor CCD design-based empirical results for PD of NFX.

3.2. RSM optimization of the CNRs

3.2.1. 4-Factor CCD design. For assortment and optimization of the significant factors modulating the PD of NFX, the 4-factor CCD-based RSM design is presented in Table S1. A total of 30 experiments were conducted by utilizing the standard table, and the acquired PD results were statistically tested against numerous models, including the linear, quadratic, cubic, and 2FI models, as presented in Table S2. The acquired results for the PD of NFX are presented in Fig. 6 using the run order. It should be mentioned here that the run order is different from the standard order of CCD, as in the case of the run order, the standard design is randomized to reduce the error probability in the PD of NFX. The maximum and minimum PD results for NFX were found to be 65.98% (conditions: reaction time = 35 min; CNRs = 10 mg L^{-1}; NFX dose = 47.5 ppm; and pH = 7.5) and 90.26% (conditions: reaction time = 40 min; CNRs = 40 mg L^{-1}; NFX dose = 65 ppm; and pH = 5), respectively, as highlighted in Fig. 5. This information is essential as the necessity of applying transformation to the acquired data is determined by the $\frac{\text{maximum PD value}}{\text{minimum PD value}}$ ratio *i.e.* if the ratio is <10.00 then no transformation is recommended, while for ratio values >10, transformation (such as square root, natural log, inverse, power, base 10 log, arcsine square root, inverse, inverse square root, or log it) is applied depending on the acquired value of the ratio. The ratio of 1.36 for PD of NFX suggested that no transformation is recommended by the software before model application of the data.[40]

The model fitting summary associated with the PD of NFX is presented in Table 3. The *p*-value is the most significant parameter determining the marginal statistical significance capability of the model with respect to the acquired PD results. The statistical significance of any model can be studied at the two different levels of 95% (*p*-value <0.05) and 99% (*p*-value <0.01) confidence interval (CI), as indicated by the corresponding *p*-values. It was observed that the quadratic model was found to exhibit the best fit in terms of the *p*-value test (*i.e.* <0.0001), as this model was found to exhibit the best fit at both the 95% and 99% intervals. Consequently, the quadratic

Table 3 Model fitting summary for the PD of NFX

Models	*p*-value	R^2	Adjusted-R^2	Predicted R^2	Standard deviation	Statistical results
Linear	0.3032	0.1703	0.0376	−0.2052	6.72	Not suggested
2FI	0.1735	0.4611	0.1774	0.0354	6.21	Not suggested
Quadratic	**<0.0001**	**0.9285**	**0.8617**	**0.7431**	**2.55**	Recommended
Cubic	0.9539	0.9456	0.7748	−5.0035	3.25	Aliased

model appeared to be the best model among all other studied models in terms of *p*-value. The regression-based terms, including R^2, adjusted-R^2, and predicted-R^2, are another indicator that can be utilized for estimating the fitting of the model. The model selected for representing the PD of NFX should lie well within the numerically confined ranges determined by the statistics. Interestingly, the cubic model produced a higher R^2 value (closer to 1; 0.9456) compared to the quadratic model (*i.e.* 0.9285); however, the software flagged the cubic model to be aliased and recommended using the quadratic model instead. The insignificant *p*-value, acquisition of a negative predicted R^2 value, and a higher difference of the adjusted and predicted-R^2 values ($\gg$0.2) resulted in aliasing of the cubic model, indicating that the cubic model exhibits undesirable effects for properly representing the PD of NFX. The quadratic model exhibited desirable results for regression-based terms, including a high R^2 (*i.e.* 0.9285), a high adjusted R^2 (*i.e.* 0.8617), an acceptable difference between the adjusted and predicted R^2 value (*i.e.* <0.2), and a desirable *p*-value. The acquisition of the lowest standard deviation of 2.55 in comparison to all other models further authenticated the validity of the quadratic model for the design space of PD of NFX.[17]

3.2.2. ANOVA analysis. The RSM-CCD-based quadratic equation generated on the basis of actual coefficient terms with respect to the mean changes documented for PD% of NFX is represented as eqn (10).

$$\begin{aligned}\mathrm{PD} = &-44.519 + 2.843X1 + 2.099X2 + 1.3084X3 + 5.3917X4 \\ &+ 0.016X1X2 + 0.004X1X3 + 0.011X1X4 + 0.0007X2X3 \\ &- 0.105X2X4 - 0.089X3X4 - 0.052X1^2 - 0.033X2^2 \\ &- 0.011X3^2 + 0.068X4^2 \end{aligned} \quad (10)$$

Although eqn (10) is considered quite effective for determining the individual parameters' impact on the response (PD%), it cannot be utilized to estimate the impact of the interaction terms. This is attributed to the fact that this equation is scaled with respect to the individual unit of each parameter, and consequently, the acquired intercept value does not lie at the center of the design space, rendering comparative analysis of the correlation among parameters ineffective. Therefore, the coded version of the equation (represented as eqn (11)) is needed.

$$\begin{aligned}\mathrm{PD} = &+86.701 - 0.031X1 + 2.16X2 + 1.70X3 - 1.44X4 \\ &+ 0.840X1X2 + 0.368X1X3 + 0.148X1X4 + 1.28X2X3 \\ &- 2.65X2X4 + 3.90X3X4 + 1.30X1^2 + 3.37X2^2 \\ &- 3.56X3^2 + 0.426X4^2 \end{aligned} \quad (11)$$

This coded equation is utilized for performing the comparative analysis of the interaction terms with respect to the responses. The coefficient analysis (Table S3) presented the variance inflation factor (VIF) analyzed for each term of the model. The VIF values for the terms were found to be as follows: X1 (1.00); X2 (1.00); X3 (1.00); X4 (1.00); X1X2 (1.00); X1X3 (1.00); X1X4 (1.00); X2X3 (1.00); X2X4 (1.00); X3X4 (1.00); $X1^2$ (1.05); $X2^2$ (1.05); $X3^2$ (1.05); and $X4^2$ (1.05). The acquisition of VIF values >1.00 for $X1^2$, $X2^2$, $X3^2$, and $X4^2$ indicated that these terms exhibited high multicollinearity and independent variables were highly correlated with each other.[41]

Adequate precision (a parameter that estimates the signal efficacy with respect to noise) was also calculated using the software. Typically, an acquisition ratio of 4.00 is regarded as acceptable, but in our study, it was found to be 12.448, which indicated that the developed model can be utilized to navigate the design space of PD of NFX. The ANOVA analysis done for the quadratic model is presented in Table 4. The acquisition of a *p*-value <0.0001 for the quadratic model implied that overall, the model was statistically significant for both CI of 95% and 99%. ANOVA is advantageous in terms of the fact that the significance of the individual terms can also be investigated using this test. It was found that at the 95% CI, the terms X2, X3, X4, X2X4, X3X4, $X1^2$, $X2^2$, $X3^2$, and $X4^2$ were found to be statistically significant. The *F*-value of 13.90 was also impressive, as such a high *F*-value suggested that there is only 0.01% probability that this value can be achieved owing to error or noise. A lack-of-fit test was also performed, indicating that an insignificant *p*-value

Table 4 ANOVA results for the acquired PD results for NFX

Source	Sum of squares	Degree of freedom	Mean square	*F*-value	*p*-value
Model[b]	1261.60	14	90.11	13.90	<0.0001
X1	0.0241	1	0.0241	0.0037	0.9522
X2[a]	112.15	1	112.15	17.30	0.0008
X3[a]	69.50	1	69.50	10.72	0.0051
X4[a]	49.77	1	49.77	7.68	0.0143
X1X2	11.29	1	11.29	1.74	0.2067
X1X3	2.18	1	2.18	0.3357	0.5709
X1X4	0.3540	1	0.3540	0.0546	0.8184
X2X3	26.21	1	26.21	4.04	0.0626
X2X4[a]	112.15	1	112.15	17.30	0.0008
X3X4[a]	242.89	1	242.89	37.47	<0.0001
$X1^2$[a]	46.44	1	46.44	7.17	0.0172
$X2^2$[a]	312.43	1	312.43	48.20	<0.0001
$X3^2$[a]	347.86	1	347.86	53.67	<0.0001
$X4^2$[a]	4.98	1	4.98	0.7689	0.3944
Residual	97.22	15	6.48		
Lack-of-fit[b]	79.84	10	7.98	2.30	0.1858
Pure error	17.38	5	3.48		
Cor total	1358.82	29			

[a] Statistically significant with respect to 95% CI. [b] Statistically insignificant.

(*i.e.* 0.1858; <0.05) was acquired in this case, which is well in accordance with the desired result, as we desire the developed model to fit the experimental data.[42] All the statistical analyses, along with the diagnostic tests (Fig. S2 and Table S4), further authenticated that the selected model was statistically reliable for representing the PD of NFX.

3.2.3. RSM and contour analysis. The ANOVA results, particularly the *p*-values acquired for each term, are essential for developing the RSM and contour plots associated with the interaction terms. It should be mentioned here that the interaction terms (including X1X2, X1X3, X1X4, X2X4m and X3X4) do not contribute equally/significantly in the design space of PD of NFX, and only those interaction terms that exhibit significant *p*-value results (*i.e.* X2X4 and X3X4) should be considered for RSM mapping. Fig. 7 represents the actual and $\pm\alpha$-based RSM and contour plots associated with the interaction term of X2X4. Fig. 7A and B represent the contour and RSM maps for the interaction term of X2X4, respectively. Both of these graphs exhibited that efficient degradation was achieved in the entire studied range of pH (*i.e.* 5.00 and 10.00), and the trend defined by the photocatalyst dose (*i.e.* CNR dose) was followed by the pH range. The acquisition of contours in place of the straight line indicated that strong correlation existed between the two terms, and their coefficient was statistically significant to modulate the PD% of NFX. The best range of CNR dose for the acquisition of high degradation values (indicated by red color) was found to be 26–40 mg L^{-1}. At the lower range of CNRs (*i.e.* 20 to 26 mg L^{-1}), the degradation was found to be slightly lower, indicating that the catalysts do not provide enough active sites to the NFX for effective degradation. The higher concentration dose provided a high chance of the activation of the CNRs (*via* UV radiation), which subsequently enhanced the degradation probability of the NFX molecules.[38] Another thing to note here is the fact that a negligible increment in the PD% was documented from 29 mg L^{-1} to 40 mg L^{-1}, indicating that this concentration of 29 mg L^{-1} can be regarded as the critical concentration of the CNRs for the reaction under study. Adding an additional dose of CNRs from the optimum concentration will not significantly impact the PD% of NFX. Therefore, CNRs should be conserved to ensure that the overall system remains economical. Fig. 7C and D represent the contour and RSM mapping associated with the $\pm\alpha$ levels of the interaction terms of X2X4. These results exhibited the predictive nature of the quadratic model, as with

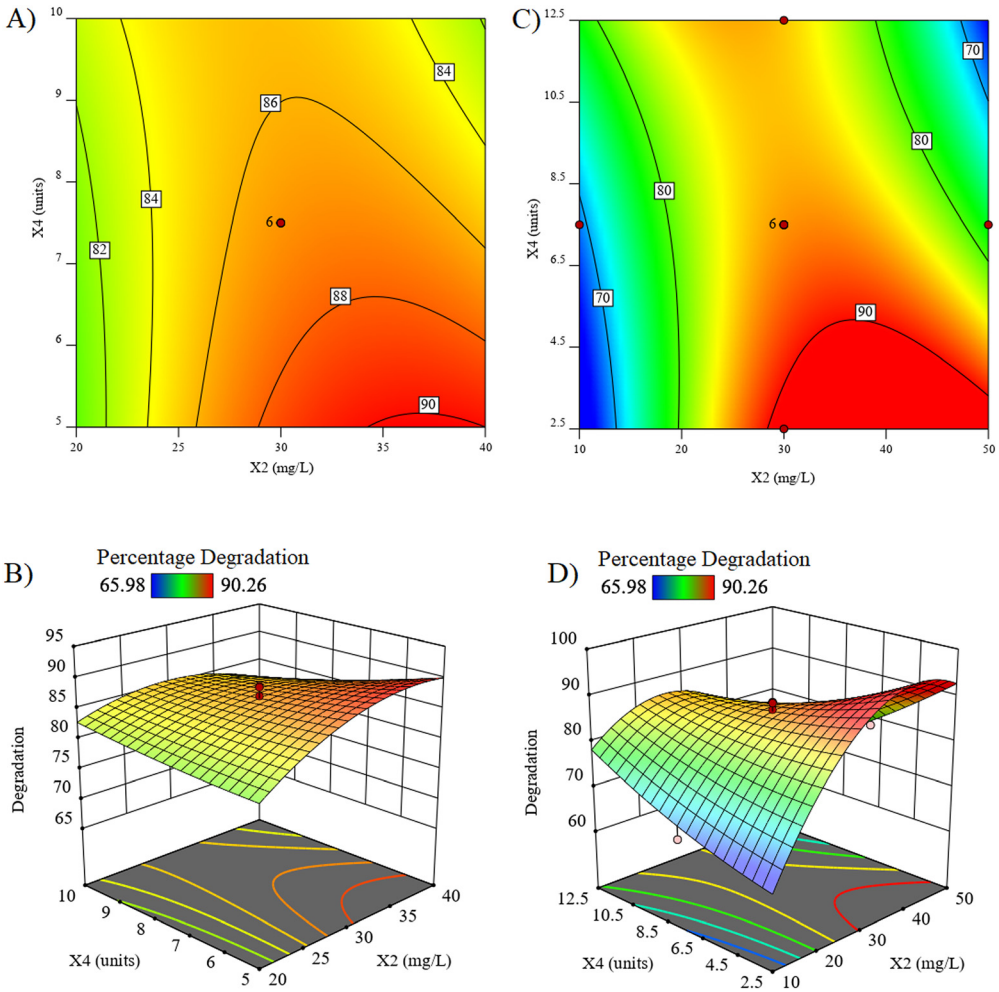

Fig. 7 (A) X2X4 contour plot; (B) X2X4 RSM plot; (C) X2X4 contour plot with respect to $\pm\alpha$; and (D) X2X4 RSM plot with respect to $\pm\alpha$.

empirical results of only ±α, the whole trend can be developed for the reaction. A similar trend was documented for these conditions, and the significance of the critical concentration of CNR dose was further highlighted as no significant increment in the PD% of NFX was documented when increasing the CNR dose by up to 50 mg L^{-1}.[32]

Similar to X2X4, the contour and RSM plots of X3X4 (represented by Fig. 8A and B, respectively) show that effective PD% values were attained for NFX at all the studied values of pH, and the acquired results were dependent on the utilized NFX dose for the reaction. It was observed that a high NFX dose (*i.e.* 39 to 65 ppm) was effectively degraded using the CNRs as indicated by the red colored region of the contour and RSM plots. This observation was highly desirable not only for laboratory experimentation but also for industrial experimentation, as effective degradation at higher doses of NFX will improve the wastewater applicability potential of the CNRs. The investigation of the contour and RSM plots of X3X4 (represented by Fig. 8C and D) with respect to ±α further validates the above-mentioned findings with respect to the pH and NFX dose parameter. The acquisition of lower PD% values at a lower dose of NFX, *i.e.* 30 to 39 ppm, is attributed to the fact the photocatalytic degradation depends upon the interaction of the generated electron (e^-) and hole (h^+) pairs with the NFX molecules.[43] At a lower dose of NFX, this probability is quite low, resulting in the acquisition of lower PD% values.[2]

The predictive power of the CCD-based quadratic model was also investigated for both terms, as presented in Fig. 9. It was observed that the higher pH values were found to be more effective in comparison to the lower pH results for both terms X2X4 and X3X4. This was attributed to the fact that the presence of a high dose of OH^- ions facilitated the generation of free radicals, which ultimately enhanced the degradation capacity of the CNRs. Another thing to note here is that the predictive model further suggested that the optimum CNR dose (Fig. 9A and B) and NFX dose (Fig. 9C and D) were required for the purpose of achieving higher degradation. Increasing the dose from the optimum ranges of CNR and NFX dose reduces the degradation efficiency, as indicated by the acquisition of green and blue regions in the graphs at higher doses of both these parameters. The predictive graph highlights the significance of RSM over OFAT for optimization of reactions, as OFAT cannot be utilized for the prediction of PD% values in the left-out ranges of the parameters.

3.3. Optimization

3.3.1. Typical optimization. The optimization process associated with the PD of NFX was assessed using the

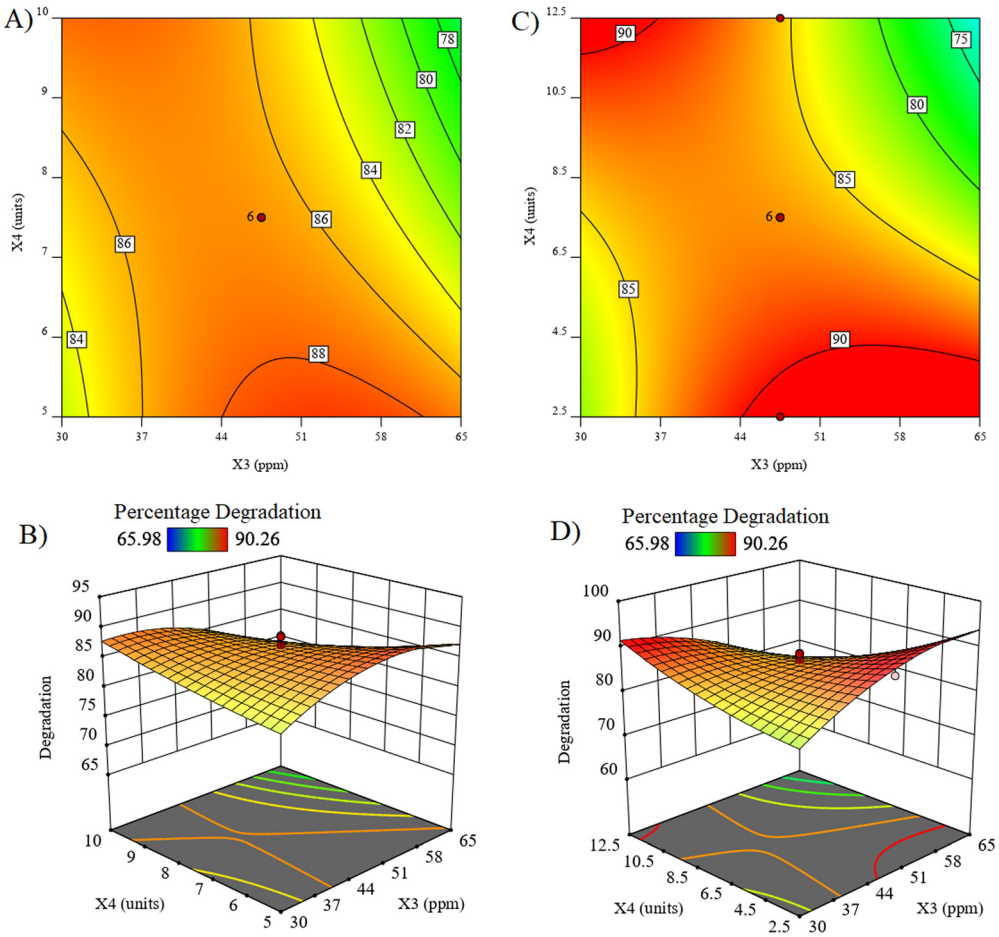

Fig. 8 (A) X3X4 contour plot; (B) X3X4 RSM plot; (C) X3X4 contour plot with respect to ±α; and (D) X3X4 RSM plot with respect to ±α.

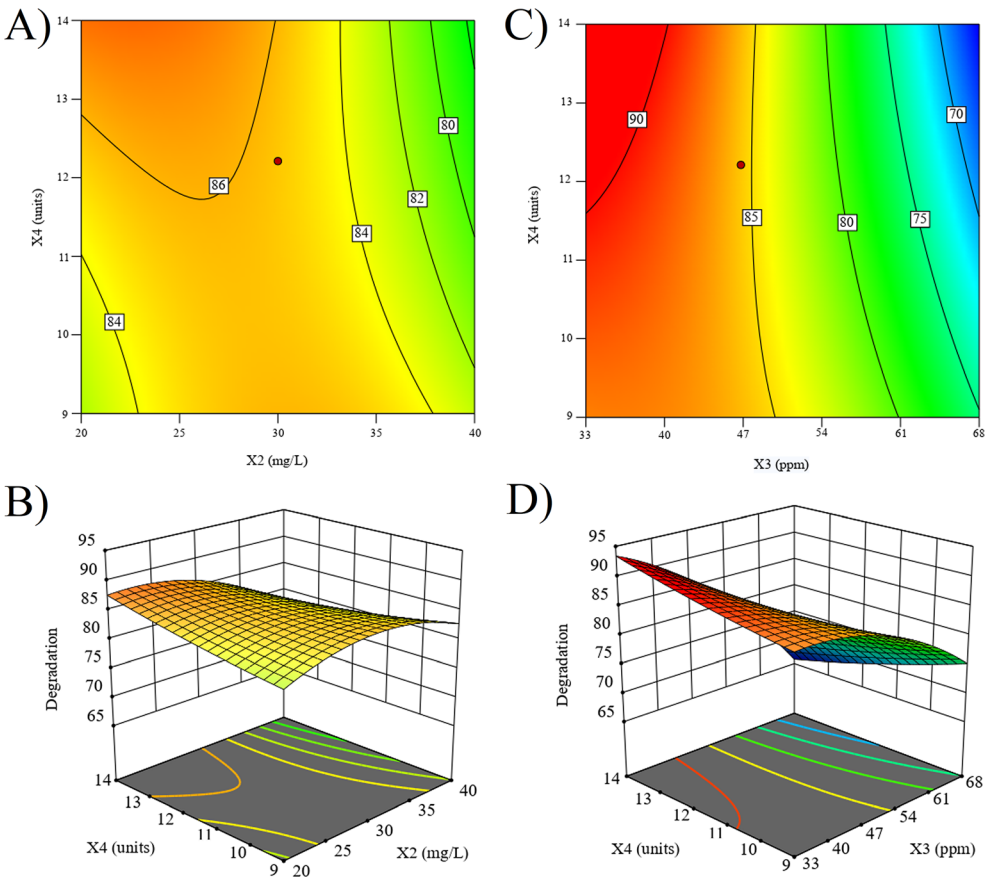

Fig. 9 (A) Predictive contour graph for X2X4; (B) predictive RSM graph for X2X4; (C) predictive contour graph for X3X4; and (D) predictive RSM graph for X3X4.

laboratory-based criterion of acquiring the maximized PD% value with the significance level of (+++++), regardless of the value of any other factor. In a laboratory setting, the reaction under study is carried out in a controlled environment with a single goal in mind—achieving the maximum degradation of the pollutant under irradiation—while all other factors (including catalyst dose, pH, NFX dose, and reaction time) were deliberately ignored. The economic implications associated with all other factors aside from PD efficacy are completely ignored, and this approach allows the calculation of the intrinsic photocatalytic efficacy of the developed CNRs.[44] As indicated in Fig. 10A, the degradation value of 90.32% was predicted *via* the CCD-based quadratic model by utilizing the parameter conditions of reaction time = 36.31 min, CNR dose = 39.56 mg L^{-1}, NFX dose = 54.52 ppm, and pH = 5.26 units. Performing the reaction under the given suggested conditions revealed that the PD% of 92.31% with the apparent rate constant value of 0.2831 min^{-1} was acquired *via* the utilization of CNRs as a photocatalyst. This observation further reinforced the effectiveness of RSM for accurately predicting the optimal conditions for certain reactions.[45]

As indicated in Fig. 10B, it was observed that the characteristic peak of NFX at 238 nm was found to continuously decrease with the increment of time, indicating that the NFX dose was continuously decreased in the medium owing to photocatalytic degradation by using the CNRs. No further decrease in the NFX dose was observed after 40 min, indicating that the reaction was completed by that time. These results were found to be comparable with the work of Chellapandi *et al.*,[46] who cited that the operational effectiveness of the PD of NFX can be greatly enhanced by the RSM approach. The RSM-based laboratory optimization approach effectively provides essential insights regarding the maximum PD efficacy that can be attained by using the developed catalyst. However, the practical aspects (including cost analysis, energy input, catalyst economic feasibility, *etc.*) associated with the real-time water treatment plants are not accounted for while implementing this approach.[47]

3.3.2. Industrial-based optimization. Unlike the laboratory approach, industrial optimization focuses on developing a holistic balance between the PD efficacy and economic feasibility. In industrial settings, the PD efficacy, along with the operational costs and scalability aspects, have to be considered, and the optimization criteria have to be expanded in this regard.[48] The following criteria were developed for achieving the optimization at the industrial scale:

(a) Main criteria: maximum PD% with significance level (+++++).

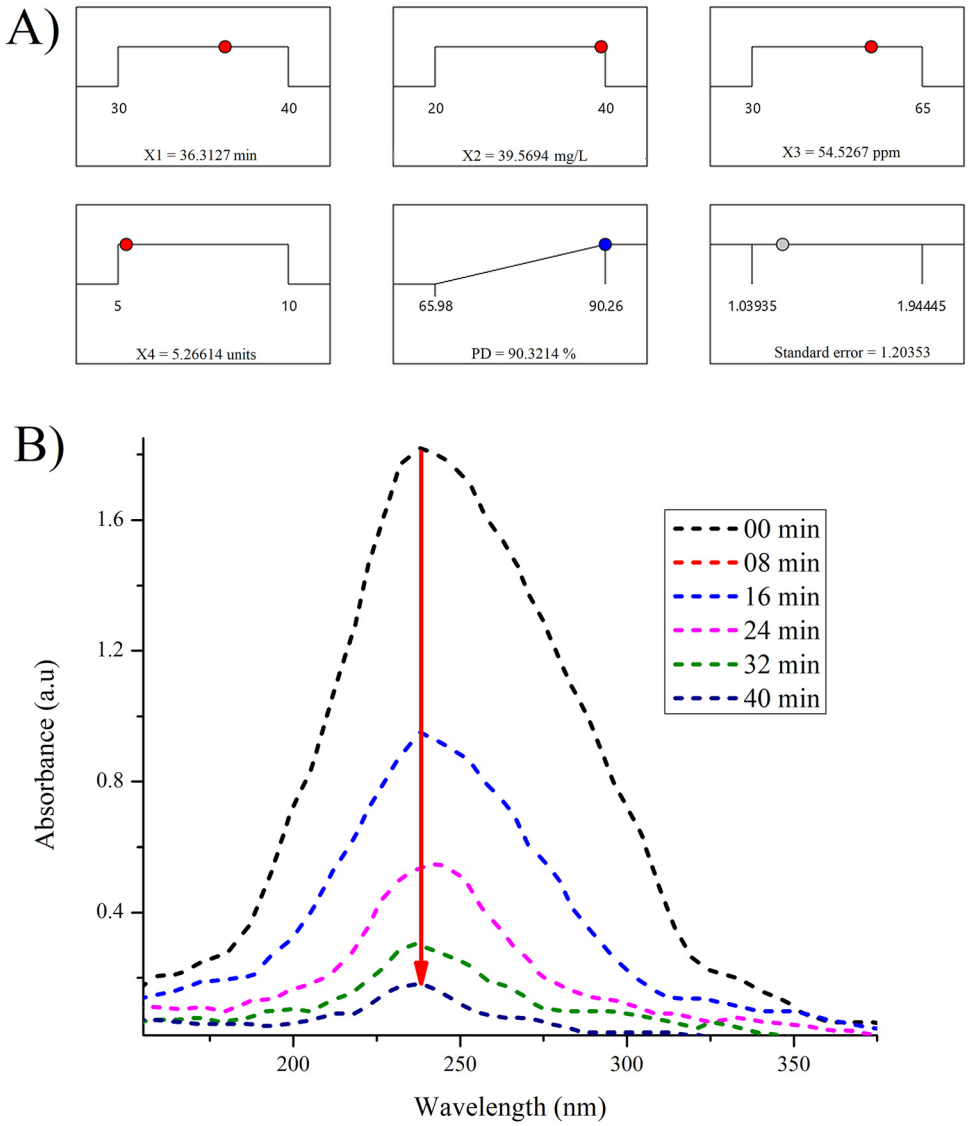

Fig. 10 (A) Ramp plot developed for the optimization of PD of NFX by using the criterion of maximum PD% with the significance value of (+++++), and (B) PD% of NFX under the optimized conditions.

(b) Maximum NFX dose with significance level (+++) aiming for maximum pollutant degradation and increasing the utility of the reaction as presented in Fig. 11A.

(c) Minimum CNR dose with significance level (+++) aiming to reduce operational cost with maximum utility as presented in Fig. 11B.

It was observed that an almost identical PD% value of 90.12% was acquired while implementing the additional criteria of maximum NFX dose. This highlighted that the acquired optimal conditions were effective in handling high pollutant loads in real-time water treatment scenarios. However, implementing the additional criterion of minimizing the CNR dose, the PD% was found to be reduced to 84.71%, which is slightly lower in comparison to the other criterion. These useful insights can be utilized by industrial owners to decide the best economic scenario for carrying out the PD% of NFX. This slight reduction may result in lower degradation, but the economic benefits associated with using minimum CNRs outweigh the marginal loss at an industrial scale. Such trade-offs are expected when optimization moves from the laboratory to industrial scale, as the former focuses on absolute performance of the catalyst while the latter focuses on striking a balance between performance and cost-effectiveness of the reaction under study.[49] The stability studies and comparative analysis of the CNRs with the academic literature are presented in Fig. S3 and Table S5, respectively.

3.4. Significance of parameters

The ANOVA results were further utilized to estimate the order of the significance of the reaction variables in the RSM-CCD-based quadratic model, as presented in Fig. 12. The SS values were utilized to estimate the TPC% value of the reaction variables. It was observed that the parameters of NFX dose and CNR dose defined the working of the CCD model by acquiring the highest

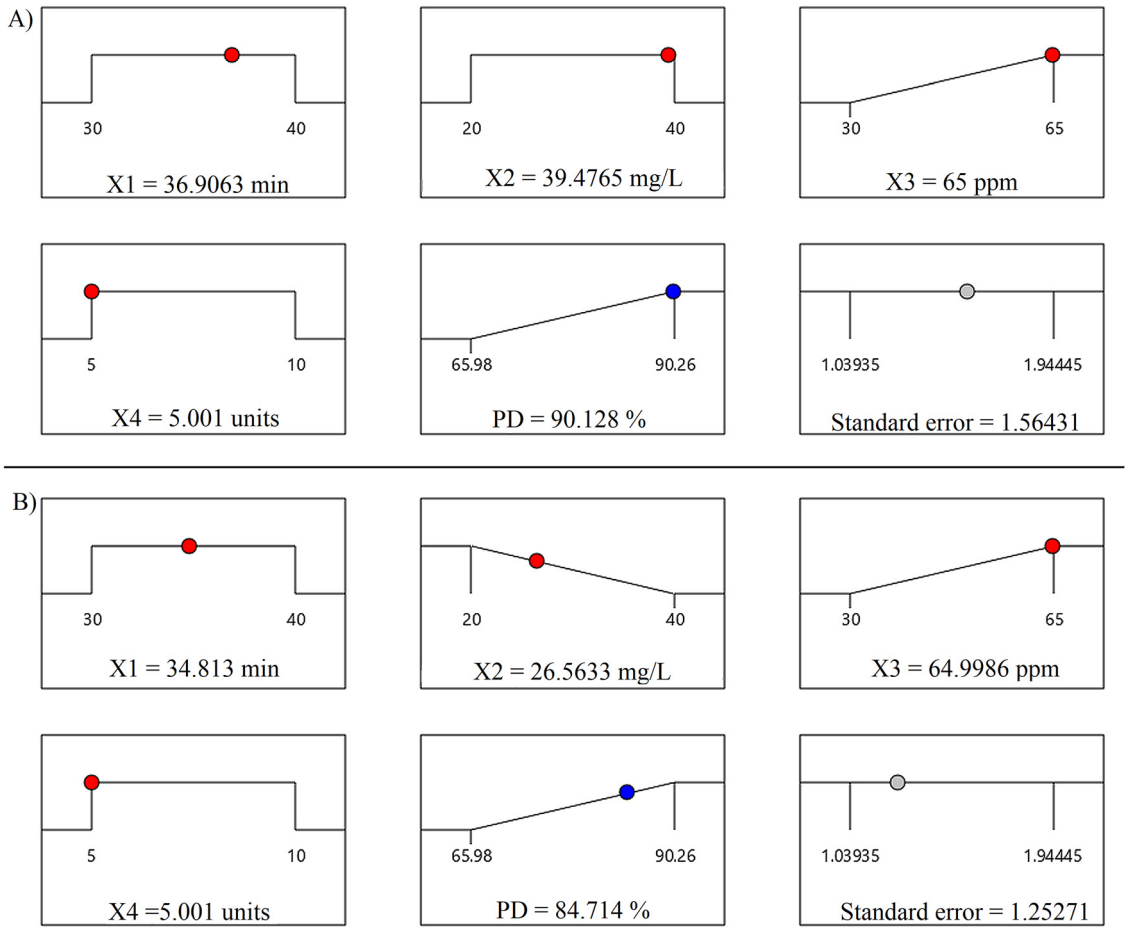

Fig. 11 Ramp plots for PD of NFX with the optimization criteria (A) maximum PD% value and maximum NFX dose; and (B) maximum PD% value, maximum NFX dose, and minimum CNR dose.

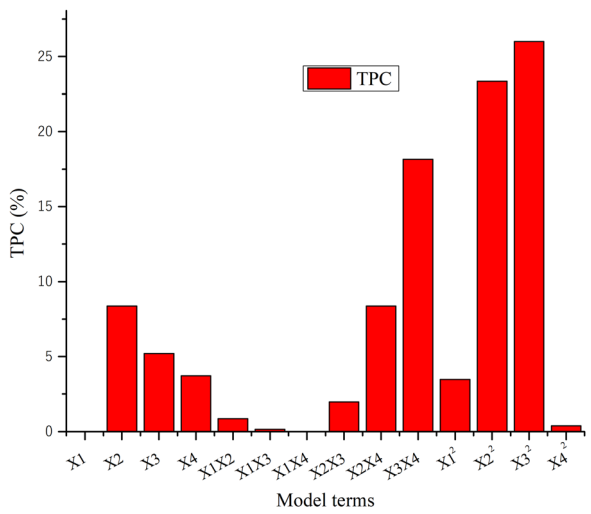

Fig. 12 TPC analysis of the CCD-RSM model for PD of NFX.

percentage contribution in the CCD-RSM model (as indicated by their quadratic and individual contribution percentages). This strongly suggested that these two variables were the primary drivers of the photocatalysis. The quadratic significance implies that there exists an optimal window for both NFX and CNR dose, and beyond these ranges, either insufficient pollutant molecules (low NFX dose) or excessive CNR dose lead to particle agglomeration/light scattering, which ultimately hinders the catalytic process.[50] This finding aligns with general photocatalytic principles, where a careful balance between active site availability and reactant loading is essential for sustaining the maximum degradation efficiency.[51] In the case of interaction terms, the terms X2X4 and X3X4 played a significant role as previously explained by the ANOVA results. The factor significance study confirms that the parameters of NFX dose and CNR dose have to be optimized to achieve higher degradation results for NFX.

4. Conclusion

The current study confirms the significance of green methodology for developing morphology-specific CNRs under facile conditions by using *Curcuma longa* extract. The novelty of the studies lies in the fact that the rod-like morphology was attained while using ambient conditions rather than extreme electro-thermal conditions. The SEM and HR-TEM results validated that CNRs with 13.1 nm mean length and 4.9 nm mean diameter were developed by using the above-mentioned

methodology. The cubic crystallographic phase and presence of a number of functional groups on the surface of the CNRs were also validated by XRD and FTIR analysis. The UV/VIS analysis of the CNRs revealed that the E_g value of the CNRs was found to be 3.64 eV, indicating that the developed photocatalyst was effective in absorbing UV region-based radiation. The PD of NFX was implemented as a model reaction for estimating the efficacy of the CNRs. The CCD-based quadratic model developed for the reaction validated that the CNRs can be effectively utilized for the degradation of persistent pollutants in the aqueous medium. In addition to performing the interaction studies, the reaction was optimized with respect to the aims of both the laboratory and industrial scales. The laboratory scale optimization revealed that the PD% of 92.31% for NFX was acquired *via* the CCD model by utilizing the parameter conditions of reaction time = 36.31 min, CNR dose = 39.56 mg L^{-1}, NFX dose = 54.52 ppm, and pH = 5.26 units. Implementing the additional industrial criteria of maximizing NFX dose and minimizing CNR dose revealed that the PD% of 84.71% was attained while considering the economic benefits alongside the maximum PD% of NFX. Such insights cannot be acquired by using conventional optimization approaches, indicating that RSM provides a robust and efficient way to optimize pollutant degradation reactions.

Conflicts of interest

The authors do not have any conflict of interest to declare.

Data availability

All the data related to the current study are available as SI. See DOI: **https://doi.org/10.1039/d5ma00717h**.

All the related data are presented in the form of figures and tables in the manuscript.

Acknowledgements

The authors acknowledge their respective institutes for providing the necessary assistance required for carrying out this research study. The authors also appreciate School of Chemistry and Molecular Engineering, East China University of Science & Technology, China for facilitating the characterization of the fabricated CNRs.

References

1 B. Li, X. Wang, A. Khurshid and S. F. Saleem, *Int. J. Environ. Sci. Technol.*, 2025, 1–14.
2 U. Fatima, H. Rafique, S. Akram, S. S. Chen, K. Naseem, J. Najeeb and M. Tayyab, *J. Cleaner Prod.*, 2024, **434**, 140003.
3 Y. Zhou, W.-B. Li, V. Kumar, M. C. Necibi, Y.-J. Mu, C.-Z. Shi, D. Chaurasia, S. Chauhan, P. Chaturvedi and M. Sillanpää, *Environ. Res.*, 2022, **211**, 113075.
4 R. Balasubramanian, N. M. P. Maideen and H. Narayanaswamy, *Ibnosina J. Med. Biomed. Sci.*, 2024, **16**(02), 29–37.
5 M. Feng, Z. Wang, D. D. Dionysiou and V. K. Sharma, *J. Hazard. Mater.*, 2018, **344**, 1136–1154.
6 X. Guo, R. Li, Y. Zhang and S. Pan, *Chem. Eng. J.*, 2024, **481**, 148468.
7 H. Yan, B. Yang, X. Zhou, X. Qiu, D. Zhu, H. Wu, M. Li, Q. Long, Y. Xia and J. Chen, *Powder Technol.*, 2022, **407**, 117611.
8 L. Han, C. Shan, C. Shuang, S. Xu, Q. Zhou, R. Ji, A. Li and Y. Pan, *Chem. Eng. J.*, 2024, **486**, 150881.
9 Y. Yang, X. Li, J. Wang and D. Song, *J. Hazard. Mater.*, 2024, 134521.
10 Q. Fang, Q. Sun, J. Ge, H. Wang and J. Qi, *Catalysts*, 2025, **15**, 477.
11 Y. Liu, J. Wei, Q. Zong, C. Chen, T. Yang and W. Liu, *Opt. Mater.*, 2024, **150**, 115158.
12 J. Mukherjee, B. K. Lodh, R. Sharma, N. Mahata, M. P. Shah, S. Mandal, S. Ghanta and B. Bhunia, *Chemosphere*, 2023, 140473.
13 M. Zou, W. Tian, M. Chu and Z. Chen, *Proc. Saf. Environ. Prot.*, 2024, **185**, 435–444.
14 J. Fan, X. Zhang, N. He, F. Song and X. Wang, *J. Environ. Chem. Eng.*, 2025, 117870.
15 D. L. Zhao, W. Zhou, L. Shen, B. Li, H. Sun, Z. Qianqian, C. Y. Tang, H. Lin and T.-S. Chung, *Water Res.*, 2024, 121111.
16 M. A. Al Masud, W. S. Shin, A. Septian, H. Samaraweera, I. J. Khan, M. M. Mohamed, M. M. Billah, E. A. López-Maldonado, M. M. Rahman and A. R. M. T. Islam, *Sci. Total Environ*, 2024, 171944.
17 S. Awais, H. Munir, J. Najeeb, F. Anjum, K. Naseem, N. Kausar, M. Shahid, M. Irfan and N. Najeeb, *J. Cleaner Prod.*, 2023, **406**, 136916.
18 S. Akram, M. W. Mumtaz, M. Danish, H. Mukhtar, A. Irfan, S. A. Raza, Z. Wang and M. Arshad, *Renewable Energy*, 2019, **143**, 898–905.
19 A. Shahzadi, M. W. Mumtaz, H. Mukhtar, S. Akram, T. Touqeer, V. Zambare and L. Christopher, *Processes*, 2021, **9**, 2012.
20 A. Fatima, M. W. Mumtaz, H. Mukhtar, S. Akram, T. Touqeer, U. Rashid, M. R. Ul Mustafa, I. A. Nehdi and M. I. Saiman, *Catalysts*, 2020, **10**, 231.
21 S. Akram, Z. Wang, L. Chen, Q. Wang, G. Shen, N. Han, Y. Chen and G. Ge, *Catal. Commun.*, 2016, **73**, 123–127.
22 P. Mahmoodi, A. Motavalizadehkakhky, M. Darroudi, J. Mehrzad and R. Zhiani, *Bioproc. Biosyst. Eng.*, 2023, **46**, 1163–1173.
23 M. Keerthana, T. P. Malini, P. Kamaraj, P. Vivekanand, R. Arulnangai, S. J. S. Kumar, S. Harikumar, N. Arumugam, A. I. Almansour and K. Perumal, *J. Taiwan Inst. Chem. Eng.*, 2023, 105118.
24 C. de Moura Strieder, D. L. P. Macuvele, C. Soares, N. Padoin and H. G. Riella, *J. Mater. Res. Technol.*, 2024, **30**, 6376–6388.
25 N. Fifere, R. Ardeleanu, F. Doroftei, M. Dobromir and A. Airinei, *Int. J. Mol. Sci.*, 2024, **25**, 681.

26 S. Awan, A. Sajjad, Z. Ali and M. Zia, *Emergent Mater.*, 2024, 1–10.
27 K. Hkiri, H. E. A. Mohamed, S. Ghotekar and M. Maaza, *Inorg. Chem. Commun.*, 2024, 112243.
28 M. Danish, H. Ayub, Z. A. Sandhu, A. Shoaib, S. Akram, J. Najeeb and S. Naeem, *Appl. Nanosci.*, 2021, **11**, 2503–2515.
29 A. B. Kunnumakkara, M. Hegde, D. Parama, S. Girisa, A. Kumar, U. D. Daimary, P. Garodia, S. C. Yenisetti, O. V. Oommen and B. B. Aggarwal, *ACS Pharmacol. Transl. Sci.*, 2023, **6**, 447–518.
30 F. Canbolat and G. Ö. Ateş, *Anatol. J. Botany*, 2023, **7**, 154–160.
31 N. K. Gunasekaran, P. P. Tumkur, N. N. Bayon, K. Prabhakaran, W. D. Arasho, J. C. Hall and G. T. Ramesh, *Energy Environ. Focus*, 2023, **7**, 83–89.
32 E. Bazrafshan, L. Mohammadi, M. NadeemZafar, A. Dargahi and F. Pirdadeh, *Arabian J. Chem.*, 2023, **16**, 104998.
33 T. Chumroenphat, I. Somboonwatthanakul, S. Saensouk and S. Siriamornpun, *Food Chem.*, 2021, **339**, 128121.
34 S. Azam, Z. Wei and R. Wang, *J. Colloid Interface Sci.*, 2022, **615**, 417–431.
35 N. Gallucci, G. Vitiello, R. Di Girolamo, P. Imbimbo, D. M. Monti, O. Tarallo, A. Vergara, I. Russo Krauss and L. Paduano, *Nanomaterials*, 2021, **11**, 542.
36 A. Amani, Z. Derikvand and M. Ghadermazi, *Iran. J. Chem. Chem. Eng.*, 2024, **43**(9), 3208–3220.
37 S. Yefimova, V. Klochkov, N. Kavok, A. Tkachenko, A. Onishchenko, T. Chumachenko, N. Dizge, S. Özdemir, S. Gonca and K. Ocakoglu, *J. Biomed. Mater. Res. Part B*, 2023, **111**, 872–880.
38 M. A. Khan, M. A. R. Siddique, M. Sajid, S. Karim, M. U. Ali, R. Abid and S. A. I. Bokhari, *Bionanoscience*, 2023, **13**, 667–685.
39 B. S. Wee, S. A. B. E. Halim and T. F. Choo, *J. Cluster Sci.*, 2024, 1–8.
40 R. Mostafaloo, M. Asadi-Ghalhari, H. Izanloo and A. Zayadi, *Global J. Environ. Sci. Manage.*, 2020, **6**, 191–202.
41 M. I. Khan, M. N. Akhtar, N. Ashraf, J. Najeeb, H. Munir, T. I. Awan, M. B. Tahir and M. R. Kabli, *Appl. Nanosci.*, 2020, **10**, 2351–2364.
42 A. Zulfiqar, M. W. Mumtaz, H. Mukhtar, J. Najeeb, A. Irfan, S. Akram, T. Touqeer and G. Nabi, *Renewable Energy*, 2021, **169**, 1026–1037.
43 K. Yang, C. Li, Q. Zhu, H. Wang and J. Qi, *Nanomaterials*, 2025, **15**, 524.
44 Z. Yu, Z. Ning, W.-Y. Chang, S. J. Chang and H. Yang, *For. Policy Econ.*, 2023, **151**, 102957.
45 K. Naseem, Z. Aqeel, A. Tahir, J. Najeeb, A. Aziz, S. U. Khan, S. Haider and K. Alam, *Polyhedron*, 2025, **274**, 117487.
46 T. Chellapandi, S. Sudharsan and M. Elamathi, *Chem. Pap.*, 2025, 1–16.
47 U. Farooq, S. T. Zahra, J. Najeeb, K. Naseem, M. E. Khan, W. Ali, M. S. Alomar, S. K. Ali, M. Hassan and W. Al Zoubi, *Sustainable Mater. Technol.*, 2025, **44**, e01377.
48 X. Wang, H. Su and X. Liu, *Sustainability*, 2025, **17**, 6313.
49 S. Ziembowicz and M. Kida, *Sustainability*, 2025, **17**, 1908.
50 Q. Gu, J. Rong, Y. Zhang, X. Zheng, Z. Zhou, Z. Li and S. Xu, *Chem. Eng. J.*, 2025, **504**, 159143.
51 S. Sambyal, V. Chauhan, P. Shandilya and A. Priye, *Catal. Sci. Technol.*, 2025, **15**, 1865–1881.